PCCP

Accepted Manuscript

ROYAL SOCIETY OF CHEMISTRY

www.rsc.org/pccp

Structural influence on the photoluminescence properties of Eu^{3+} doped Gd_3MO_7 (M = Nb, Sb, Ta) Red Phosphors

Linda Francis T. [1], P. Prabhakar Rao[1]*, Mariyam Thomas[2], Mahesh S.K. [1], Reshmi V. R, [1] Sreena T.S. [1]

[1]Materials Science and Technology Division, CSIR - National Institute for Interdisciplinary Science and Technology (NIIST), Trivandrum – 695 019, India

[2]Department of Physics, St. Therasa's College, Ernakulam - 682011, Kerala, India

Abstract

New red phosphor materials of general formula $Gd_{3-x}MO_7$: xEu^{3+} (M = Nb, Sb, Ta) were prepared using a high temperature solid state reaction route. Detailed structural studies using XRD, FT-IR and Raman spectroscopy techniques showed that niobate and tantalate samples crystallized in the weberite type structure whereas the antimonate sample in the fluorite structure. Photoluminescence properties of the three compositions are correlated with their crystal structures. It was observed that more ordering occurs in the lattice when M site is doped from Sb to Nb to Ta. Although niobate and tantalate samples possess similar structures more distortions were noticed in the tantalate sample increasing the radiative transition probabilities. Due to the more ordered structure of Gd_3TaO_7 host lattice resulting in the more uniform distribution of Eu^{3+} ions, tantalate system showed better luminescence properties. The variation in the luminescence intensity with various Eu^{3+} concentrations in Gd_3TaO_7 host lattice was also studied to calculate the optimum doping concentration.

* Corresponding author. Tel.: + 91 471 2515311; Fax: + 91 471 2491712

Email ID: padala_rao@yahoo.com (P. Prabhakar Rao)

Introduction

Luminescence properties of the various phosphor materials highly depend on the crystallographic structures of the host lattice and the nature of the activator ion.[1,2] Thus choosing the host lattice and the activator ions as well as understanding the chemistry and the structure plays a crucial role in the phosphor synthesis. The fluorite structure (AO_2) is considered to be one of the most flexible for its ability to construct superstructures or derivatives. Pyrochlore and weberite which are anion-deficient fluorite-related structures ($A_2B_2O_7$), also maintain the closed-packed cation layers as in the fluorite structure.[3] If the four tetravalent metal ions in the A and B sites are replaced by three trivalent ions (Ln) and one pentavalent ion (M), one oxide vacancy is formed per fluorite cell. Due to the significant differences in radii between the Ln^{3+} and M^{5+} ions, cation ordering occurs on the metal sites and the oxide-vacancy orders on the anion sites.[4] Depending on the Ln^{3+} and M^{5+} ions there is a wide possibility of almost similar structures with different ordering and defect formation.

The most widely used activator for red luminescence in the phosphor materials are europium ions (Eu^{3+}) due to its high lumen equivalent, quantum efficiency, and photostability at the same time.[5,6] It is known that the probability of electronic transitions from the lowest $^5D_0$ excited state to the $^7F_{0\text{-}6}$ ground states differs depending on site symmetries.[7] Despite extensive studies on various phosphor systems there are limited understanding on the dependence of luminescence properties on the local structures and distributions of activator ions in the host lattice. However the photoluminescence spectra provides invaluable information about the nature of the doping sites and dopant locations in the host lattice.[8] Asymmetric ratio which is the ratio of the integrated intensities of electric dipole and the magnetic dipole transitions provides an estimate to the degree of local distortion and the nature of the doping sites.[9] Another informative spectral feature for assessing the local environment of Eu^{3+} ions is the $^5D_0 \rightarrow {}^7F_0$ transition which occurs

between these non-degenerate levels in 577-584 nm range. Splitting in this transition points out the dual or more non equivalent site occupancy of Eu^{3+} ions.[10] The distribution of Eu^{3+} ions in bulk compounds has been a subject of experimental and theoretical interest. Reports clearly reveal the fact that the luminescence emission intensity is higher for the more ordered structures due to the more uniform distribution of the activator ions and due to the reduced non radiative decay pathways.

Crystallographic investigations on Ln_3MO_7 can be found dating as far as back 1964.[11] Since then, there have been considerable discrepancies between various studies on the crystal structure of Ln_3MO_7 reported in literature. There have been numerous studies focusing mainly on the crystallographic aspects and the dielectric properties of the compounds like Ln_3IrO_7, Ln_3MoO_7, Ln_3RuO_7, Ln_3NbO_7, Ln_3TaO_7, Ln_3SbO_7 etc.[12,13,14] However most of them are reported as defect – fluorite superstructures. Ordering and the oxygen vacancies depend on the Ln^{3+} and M^{5+} ions. The spectroscopic properties of the doped rare earth ions usually have great influence on the local structures, co-ordination numbers, ordering and degree of distortion due to defects in the host. The luminescence properties of the compounds with Ln_3MO_7 host lattices are less reported. Recently Yanyan et.al studied the luminescence properties of hydrothermally synthesized Lu_3TaO_7, Lu_3NbO_7 and Y_3TaO_7 nanophosphors and reported them as red phosphor candidates for WLEDs upon further improvements.[15] However the compounds of general composition Ln_3MO_7 are gaining attraction and form interesting candidates as the host materials for phosphors. [16]

In light of the great importance of the host structure in the red luminescence of Eu^{3+}, the aim of the present work is to explore the structure of Ln_3MO_7 compounds and to study the distribution and the photoluminescence properties of Eu^{3+} ions in relationship with their structural properties. In this paper we have presented the luminescence properties of Eu^{3+} activated Gd_3MO_7 (M = Nb,

Sb, Ta). The variation in the luminescence intensity with various Eu^{3+} concentrations in Gd_3TaO_7 host lattice was also studied.

Experimental

Synthesis

The phosphors $Gd_{3-x}MO_7$: xEu^{3+} (M = Nb, Sb, Ta; x = 0.05, 0.10, 0.15, 0.20) were prepared by a high temperature solid state reaction route. Gd_2O_3, Nb_2O_5, Sb_2O_5, Ta_2O_5 and Eu_2O_3 (Sigma Aldrich, 99.99%) were used as the starting materials. Chemicals were weighed in the stoichiometric ratio and then finely ground and mixed in an agate mortar in acetone medium with intermittent drying. The homogeneous mixture was calcined on an alumina plate at 1400ºC for 6 hours twice powdering and pelletizing after the first calcination.

Characterization

The crystalline structure of the samples was examined with an X - ray powder diffractometer (X'Pert Pro PANalytical, operated at 40 kV and 30 mA, Cu - Kα = 1.5406 Å, 2θ range = 10 - 90°). The FT Raman spectra of the powdered samples were recorded on a Labram HR 800 (Horiba Scientific, Instrument no L/4/794) spectrometer using argon laser excitation (784nm). Fourier transform infrared spectroscopy (FT–IR) data were collected on a (Perkin-Elmer Spectrum One FT-IR Spectrometer) over the range of wavenumber 4000–400 cm^{-1}, and the standard KBr pellet technique was employed. Morphological studies of powder particles were done by a scanning electron microscope (JEOL, JSM-5600LV) operated at 15kV. EDS spectra was also recorded to identify the elements present. Absorbance study of the samples were carried out using a Shimadzu, UV - 2450 UV-Vis spectrophotometer in the 400 –700 nm wavelength range using barium sulfate as a reference. The excitation and emission spectra were recorded on a Fluorolog HORIBA fluorescence spectrophotometer with a Xenon lamp (450 W) as the excitation source. Luminescence life time of the phosphors was recorded by the phosphorimeter

attached to Fluorolog®3 spectrofluorimeter. All the measurements were carried out at room temperature.

Results and Discussion

Structural Studies

Powder X - Ray diffraction patterns of $Gd_{2.85}MO_7$:*0.15*Eu^{3+} (M = Nb, Sb, Ta) are shown in the Figure1. All the samples seemed to match well with a cubic fluorite profile at the first glance. After detailed observation it was found that both $Gd_{2.85}NbO_7$:*0.15*Eu^{3+} and $Gd_{2.85}TaO_7$:*0.15*Eu^{3+} powder diffraction patterns contains more minor peaks with intensities below 5% of the relative intensity which cannot be attributed to the cubic fluorite or pyrochlore structure and can be correctly indexed on the basis of the Gd_3TaO_7 compound (JCPDS No: 00-038-1409). Yokogawa et al. has earlier described the structure as a weberite type with a space group *C*2221.[17] The characteristic of this family of weberite is that MO_6 are corner linked to each other and form chains of MO_6 octahedra with parallel chains of LnO_8 distorted cubes. Thus in a weberite structure there are equal numbers of VI and VIII coordinated cations in an ordered BO_6 - AO_8 layer arrangement.[18] In the case of orthorhombic structures the possibility that the LnI and LnII cations may be of different types, the VIII coordinated and VII coordinated can also be realized. The cation ordering in this specimen may not be complete. In our case, the degree of ordering in tantalate and niobate sample may be different.[19] It is noticed that the powder XRD pattern of $Gd_{2.85}SbO_7$:*0.15*Eu^{3+} matched well with cubic fluorite structure (JCPDS No: 01-074-6419, Space group: F*m*-3*m*). Rietveld refinements of the above three samples were carried out for the detailed structural studies. Starting models used for the refinement are given in the tables I and II.[20] In all the three cases Eu^{3+} is expected to occupy the Gd^{3+} site considering the matching ionic radius and the coordination numbers of the ions.[21] The profile was fitted using a Pseudo Voigt profile function. The observed, calculated and the difference powder diffraction profiles of the samples

(M = Nb, Sb, Ta) are given in supporting information Figures S1, S2, and S3 respectively. Table III gives the refined values of all the three samples. The refined R values suggest that the refinement is in good agreement with the space group in all respects. Selected bond distances of the atoms obtained from the Rietveld analysis are given in the Table IV. A small increase in the bond distances and a corresponding lattice expansion is observed in the tantalate system in comparison with the niobate system. This is attributed to the slight difference in the electronegativity of the two cations. Electronegativities of tantalum and niobium are 1.5 and 1.6 respectively. Schematic representation of the crystal structure and the coordination polyhedra of the tantalate sample generated using the diamond software is given in the Figure 2. (see supporting information Figure S4 for the crystal structure and the coordination polyhedra of the niobate sample)

FT - IR spectra of the three samples are given in the Figure 3. As expected from the XRD analysis niobate and tantalate samples showed similar modes of vibrations whereas the antimonate sample possessed totally different type spectra. It is predicted that the higher the ratio of formula volume to Ln^{3+} ionic radius higher the probability of polar distortions.[22] The presence of more IR vibrational peaks in the tantalate sample is thus attributed to the higher distortions in the structure owing to "looseness" of the system which can also be related to the increased bond lengths. It is known that a vibration to be IR active there must be change in the dipole moment vector. Thus from the FT-IR spectra it can be understood that the tantalate system possess more bonds associated with a net dipole moment change. According to Cia et al. larger unit cell volume probably contributes a greater BO_6 distortion.[23] Thus the FT-IR results indirectly points to the possibility that the Eu^{3+} ions may be located in an more distorted site in the case of tantalate system than in the case of the niobate system.

Further confirmation of the structures of the three samples was done by recording the FT - Raman spectra of the samples. Figure 4 gives the FT - Raman spectra of the samples. The Raman spectra of $Gd_{2.85}SbO_7$:*0.15*Eu^{3+}clearly revealed the fluorite structure of the compound.[24] In Raman studies also niobate and tantalate samples showed similar modes of vibrations which correspond to the weberite structure with some variation in the intensity.[25] But the observation was that some minor modes which were not present in the niobate sample were observed in the tantalate sample. According to Kovyazina et al., in the weberite structure, 24 modes are Raman active: $5A_{1g} + 5B_{1g} + 7B_{2g} + 7B_{3g}$. Oxygen redistribution in the lattice leading to the formation of different polyhedra of different coordination can lead to presence or absence of some modes in the Raman spectra. The sharper and intense lines in the Raman spectra of the tantalate sample indicate the redistribution of oxygen in the sample due to some distortions resulting in the presence of more Raman vibrational modes. The high frequency line $\nu_1(A_{1g})$ at 764 cm^{-1} (tantalate) and 779 cm^{-1} (niobate) sample corresponds to the stretching vibrations of Nb/Ta-O bonds in the Nb/TaO_6 octahedra. The shift in the lines towards the higher frequencies may be caused by the shorter Nb - O bonds in the NbO_6 octahedra in comparison with that of TaO_6 octahedra which is again in agreement with the smaller lattice parameter values of niobate samples obtained from the Rietveld results. Again the $\nu_1(A_{1g})$ line is very sensitive to the structural ordering. The lines are weaker for the disordered structures.[26] This points out to the more ordered nature of the tantalate system. Thus some distortions and the more ordered nature of the tantalate system that could not be well detected from the XRD studies could be identified from both FT-IR and FT-Raman studies.

Morphological Studies

Typical scanning electron micrographs of the three samples $Gd_{2.85}MO_7$:*0.15*Eu^{3+} (M = Nb, Sb, Ta) are given in Figure 5. All three samples were slightly agglomerated and the particle sizes are

in between 0.5 - 1μ. EDS spectra of the three samples were recorded and the atomic mass percentages were found to be in well agreement with the theoretical stoichiometry (see supporting information Figures S5, S6 and S7). X-ray dot mapping of the samples were also carried out to study the distribution of atoms and are given in the supporting information Figures S4, S5 and S6.

Photoluminescence Properties

Photoluminescence properties of all the samples were studied and the excitation and emission spectra of three typical samples are given in the Figures 6 and 7 respectively. Broad band in the excitation spectra ranging from 240 – 325 nm corresponds to the overall combination of charge transfer transition in metal - oxygen polyhedron of the compound.[27] The narrow peaks beyond CTB correspond to the intra configurational 4f – 4f transitions of Eu^{3+} ions in the host lattice. The most intense peaks at 394 and 464 nm is assigned to $^7F_0 \rightarrow {}^5L_6$ and $^7F_0 \rightarrow {}^5D_2$ transitions respectively.[28] Niobate sample has broader and less intense CTB with maximum at 294nm in the near UV region in comparison with antimonate (278nm) and tantalate (272nm) system. The red shift of the CTB in the case of niobate sample is related to the lower ionization potential of niobium (6.88V) in comparison with tantalum (7.89V). Higher absorption of the niobate sample in the UV region is understood from the absorption spectrum (inset of the figure 6). Absorption spectra of all the three samples shows good absorption in the UV region pointing to the applicability of these phosphor materials with UV led chip. In the niobate sample the intensity of the f-f transitions are more intense than the charge transfer band. Similarly in the case of the tantalate system the f-f transitions are more intense than the CTB. However, $Gd_{2.85}SbO_7$:*0.15*Eu^{3+} shows very weak excitation spectra than the other two samples. This can be related to the fluorite structure of antimonate sample which is more disordered structure than the weberite leading to the non uniform distribution of Eu^{3+} ions. Also it is inferred that SbO_8 is less

effective in transferring energy to the activators when compared to NbO_6 and TaO_6 groups. Unlike the tantalum and niobium systems CTB is much higher than the f-f transition peaks.

The emission profiles of the three samples are different. The emission intensities under an excitation wavelength of 394 nm were in accordance with the intensities of the $^7F_0 \rightarrow {}^5L_6$ transition peaks in the excitation spectrum. The asymmetric ratio (ratio of electric dipole and magnetic dipole transitions) provides information about the site occupancy of Eu^{3+} ions in the gadolinium sites. Better asymmetric ratio of the tantalate (2.8) sample shows the slightly better occupancy of Eu^{3+} ions in more non-centro symmetric sites in comparison with the niobate sample (2.4). To examine the details of the site distribution of Eu^{3+} ions $^5D_0 \rightarrow {}^7F_0$ transition under 394nm excitation was investigated in detail and no evident split was observed indicating the occupancy of Eu^{3+} ions in a single site, mostly an 8 coordinated site. The probability of electric dipole transitions ($^5D_0$ - $^7F_2$) is rapidly promoted when the doped Eu^{3+} ions is occupied at a highly distorted 8 coordinated sites. Thus in the tantalate system Eu^{3+} being located at a more distorted site than the niobate sample the probability of ED transitions is higher. It is clear from the spectra that the tantalate samples show maximum emission intensity which is more than twice (2.4 times) the niobate system. Bond distances also plays crucial role in the luminescence intensity of the phosphor materials. This phenomenon is attributed to the crystal field effect. When the Ln-O bond is short (strong crystal field effect), it could favour the energy transfer which harms the luminescence from Eu^{3+} - Eu^{3+} f-f transitions. [27] It could be suggested that the detailed understanding on the site distribution and the host structure is needed for the deeper analysis of the luminescence mechanisms.

The decay curves for $^5D_0$ - $^7F_2$ transition (612 nm) of $Gd_{2.85}MO_7$:*0.15*Eu^{3+} (M = Nb, Ta) under near UV excitation are shown in Figure 8. Decay curve of the antimonate sample was not

recorded since the sample had very weak orange - red emission. Both the decay curves can be fitted well with a single exponential function given as;

$$I = A \exp(-x/\tau)$$

where, I, τ and A are intensity, decay time and fitting parameter respectively. The lifetime was obtained as 0.64 ms for niobate sample and 0.79 ms for tantalate system. The decay lifetimes (τ) is proportional to the transition probability. Heavier distortion of the crystallographic sites usually denotes the higher transition probability of Eu^{3+} ions. Thus the higher lifetime of the tantalate sample further confirms the more uniform distribution of Eu^{3+} ions in the Gd_3TaO_7 lattice. The defects in the weberite structure of the niobate samples also produces more non radiative decay pathways reducing the lifetime.[29] From the excitation, emission and lifetime spectra tantalate sample was showing better luminescence properties and thus further studies were confined to that system.

Effect of Eu^{3+} doping in Gd_3TaO_7 host lattice

Powder X - Ray diffraction patterns of $Gd_{3-x}TaO_7$:xEu^{3+} (x = 0.05, 0.1, 0.15, 0.2) given in the Figure 9 reveal the crystallinity and phase purity of all the samples and they are in good agreement with the powder diffraction pattern of weberite Gd_3TaO_7 compound (Space group: *C*2221; JCPDS No: 00-038-1409). The substitution of the Gd^{3+} ion (1.05 Å, co-ordination number, CN = 8) by slightly larger Eu^{3+} ion (1.066 Å, CN = 8) results in the lattice expansion, which is confirmed by the shift of XRD peaks of $Gd_{3-x}TaO_7$: xEu^{3+} towards the lower 2θ angle side with increasing Eu^{3+} content.[30] The shift of the XRD pattern towards left is shown in the inset of Figure 9. No impurity peaks were seen with increasing doping concentration Eu^{3+} in the Gd_3TaO_7 lattice.

Critical influence of the activator concentration in the luminescence intensity was studied and the recorded excitation and emission spectra of $Gd_{3-x}TaO_7$: xEu^{3+} (x = 0.05, 0.1, 0.15, 0.2) is shown in the Figure 10. Increase in the Eu^{3+} content doesn't change the shape and peak positions of the excitation and emission spectra although the intensity changes. The variation of emission intensity of $Gd_{3-x}TaO_7$: xEu^{3+} with Eu^{3+} doping concentration under 394 nm is shown in Figure 11. At low concentration ranges (up to x = 0.15) the luminescence intensity gradually increases with doping content as multiphonon and cross relaxation processes are the major reasons for the electrons in the excited states to enter the $^5D_0$ level. When the distance between the Eu^{3+} ions satisfies the Dexter and Forster resonant energy transfer condition, concentration quenching happens. By further increase in the doping concentration, energy transfer processes known as second-order interactions and spin relaxation occur easily between the coupled excited Eu^{3+} ions resulting in the decline of luminescence intensity.[31-33] Thus the emission intensity decreases with further increase in the doping concentration. Similar emission profiles with slightly lesser intensities were obtained under 464 nm excitation. The decay curves of all the samples are given in Figure 12 and the lifetime values with increasing concentrations from x = 0.05 to x = 0.2 are 0.95, 0.82, 0.79 and 0.75 ms respectively.

Conclusions

In summary, the detailed structural and optical studies of three systems with general formula Gd_3MO_7 were carried out. Studies revealed that the tantalate sample showed better luminescence properties in terms of emission intensity, asymmetric ratio, and lifetimes. It was noticed that degree of ordering in the crystal structure as well as the local distortions in the luminescent sites plays crucial roles in the luminescence properties. The variation in the luminescence intensity with Eu^{3+} concentrations was studied in Gd_3TaO_7 host system and the doping concentration was optimized. The excitation and emission spectra of the prepared samples indicate that phosphor

material can be effectively excited by UV and blue light (394 and 464 nm) and it exhibits intense red emissions, nicely fitting in with the widely applied UV and blue LED chips.

Acknowledgement

One of the authors, Linda Francis T., would like to acknowledge the Council of Scientific Industrial Research (CSIR), Govt. of India, for the financial support towards a senior research fellowship.

References

1. P. S. Dutta and A. Khanna, J. Solid State Sci. Technol. 2, R3153 (2013).

2. G. Blasse and B. C. Grabmeyer, Luminescent Materials., Springer, Berlin, 1994.

3. Cai L and Nino JC, Acta Crystallogr B. 65, 269 (2009).

4. Subramanian, M. A., Aravamudan, G. and Rao, Prog. Solid State Chem. 15, 55 (1983).

5. C. Ronda, Luminescence from Theory to Applications, Wiley-VCH Verlag GmbH & Co. KGaA, Weinheim, 2008.

6. Mihail Nazarov and Do Young Noh, New Generation of Europium and Terbium Activated Phosphors: From Syntheses to applications, Pan Stanford Publishing, Pte. Ltd., Singapore, 2011.

7. Fujihara S and Tokumo K, Chem Mater. 17, 5587 (2005).

8. J.C.G. Bünzli, G.R. Choppin, Lanthanide probes in life, chemical and earth sciences: Theory and practice, Elsevier, New York, 1989.

9. C. Gorller-Walrand, K. Binnemans, Rationalization of Crystal-Field Parametrization. In Handbook on the Physics and Chemistry of Rare Earths, ed. K. A. Gschneidner Jr., L. Eyring, North-Holland, Amsterdam, 23, 1996.

10. K. Binnemans and Gorller-Walrand, J. Rare Earths. 14, 173 (1996).

11. Rooksby, H. P. and White, E. A. D., J. Am. Ceram. Soc. 47, 94 (1964).

12. G. Tilloca, M.Perez and Y. Jorba, Comp. Rend. acad. Sci. 271, 134 (1970).

13. Lu Cai and Juan C Nino, J. Solid State Chem.184, 2263 (2011).

14. Nobuo Ishizawa, Kenji Tateishi, Saki Kondo and Tsuyoshi Suwa, Inorg. Chem. 47, 558 (2008).

15. Yanyan Du, Yuan Zhang, Keke Huang, Shan Wang, Long Yuan and Shouhua Feng. Dalton Trans. 42, 8041 (2013).

16. Jing Wang, Yu Cheng, Yanlin Huang, Peiqing Cai, Sun Kim and Hyo Jin Seo, doi 10.1039/C4TC00359

17. Yokogawa Y., Yoshimura M., and Somiya S., Solid State Ionics. 35, 275 (1989).

18. Lu Cai, Sava Denev, Venkatraman Gopalan, and Juan C. Nino, J. Am. Ceram. Soc. 93, 875 (2010).

19. T. Fennell, S. T. Bramwell and M. A. Green , Can. J. Phys, 79, 1415 (2001)

20. H. J. Rossell, J. Solid State Chem. 27,115 (1979).

21. Shannon R, Acta Cryst.A. 32, 751 (1976).

22. Lu Cai and Juan C. Nino, J. Eur. Ceram. Soc. 27, 3971 (2007).

23. Lu Cai and Juan C. Nino, J. Eur. Ceram. Soc. 30, 307 (2010).

24. Marianne Glerup, Ole Faurskov Nielsen and Finn Willy Poulsen, J. Solid State Chem. 160, 25 (2001).

25. S. A. Kovyazina, L. A. Perelyaeva, I. A. Leonidov and Yu. A. Bakhteeva, J. Struct.Chem. 44, 975 (2003).

26. Nicolas Preux, Aure lie Rolle, Cindy Merlin, Messaoud Benamira, Marcin Malys, Claude Estournes, Annick Rubbens and Rose-Noe lle Vannier, C.R. Chim. 13, 1351 (2010).

27. Xin Yin, Yaoming Wang, Fuqiang Huang, Yujuan Xia, Dongyun Wan and Jiyong Yao, J. Solid State Chem. 184, 3324 (2011).

28. Blasse, G.; Karl, A. Gschneidner, J. a. L. E. Chemistry and physics of R-activated phosphors. In Handbook on the Physics and Chemistry of Rare Earths; Elsevier: Amsterdam, 1979.

29. William M. Yen, Shigeo Shionoya and H. Yamamoto, (Phosphor Handbook, 2006).

30. L. Vegard, Zeitschrift fur Physik. 5, 17 (1921).

31. de Dood M. J. A., Knoester J., Tip A., Polman A., Phys Rev B. 71, 115102 (2005).

32. Tallant D R, Seager C H and Simpson R. L., J. Appl Phys. 91, 4053 (2002).

33. Krupa J. C., J. Solid State Chem. 178, 483 (2005).

Table and Figure Captions

TABLE I. Starting model of $Gd_{2.85}MO_7$:*0.15*Eu^{3+} (M = Nb, Ta)

TABLE II. Starting model of $Gd_{2.85}SbO_7$:*0.15*Eu^{3+}

TABLE III. Refined parameters of Rietveld analysis of $Gd_{2.85}MO_7$:*0.15*Eu^{3+} (M = Nb, Sb, Ta)

TABLE IV. Selected bond distances of $Gd_{2.85}MO_7$:*0.15*Eu^{3+} (M = Nb, Ta)

FIG. 1.Powder X-ray diffraction patterns of $Gd_{2.85}MO_7$:*0.15*Eu^{3+} (M = Nb, Sb, Ta).

FIG. 2.Schematic representation of the crystal structure and the coordination polyhedras of $Gd_{2.85}TaO_7$:*0.15*Eu^{3+}.

FIG. 3.FT - IR Spectra of $Gd_{2.85}MO_7$:*0.15*Eu^{3+} (M = Nb, Sb, Ta) samples.

FIG. 4.FT - Raman Spectra of $Gd_{2.85}MO_7$:*0.15*Eu^{3+} (M = Nb, Sb, Ta) samples.

FIG. 5.Scanning electron micrographs of $Gd_{2.85}MO_7$:*0.15*Eu^{3+} M = Nb (a), Sb (b), Ta (c).

FIG. 6.Photoluminescence excitation spectrum of $Gd_{2.85}MO_7$:*0.15*Eu^{3+} (M = Nb, Sb, Ta) for an emission at 612 nm (Inset: UV - Visible absorption spectrum of the samples).

FIG. 7.Photoluminescence emission spectra of $Gd_{2.85}MO_7$:*0.15*Eu^{3+} (M = Nb, Sb, Ta) under 394 nm excitation.

FIG. 8.Decay curves of Eu^{3+} emission at 612 nm in $Gd_{2.85}MO_7$:*0.15*Eu^{3+} (M = Nb, Ta) under 394 nm excitation.

FIG. 9.Powder X-ray diffraction patterns of $Gd_{3-x}TaO_7$: *0.15*Eu^{3+} (x = 0.05, 0.1, 0.15, 0.2).

FIG. 10.Photoluminescence emission spectra under 394 nm excitation and excitation spectrum for an emission at 612 nm of $Gd_{2.85}TaO_7$:$x$$Eu^{3+}$

FIG. 11.Variation in luminescent intensities of $Gd_{3-x}TaO_7$:$x$$Eu^{3+}$ (x = 0.05, 0.1, 0.15, 0.2) with Eu^{3+} doping concentrations

FIG. 12.Decay curves of Eu^{3+} emission at 612 nm in $Gd_{3-x}TaO_7:xEu^{3+}$ (x = 0.05, 0.1, 0.15, 0.2) under 394 nm excitation.

TABLE I. Starting model of $Gd_{2.85}MO_7$:*0.15*Eu^{3+} (M = Nb,Ta)

Element	Wyckoff	*x*	*y*	*z*	Sof
Gd	4b	0	0.4954	0.25	0.85
Eu	4b	0	0.4954	0.25	0.15
Gd	8c	0.2338	0.2349	0.002	1
Nb / Ta	4b	0	-0.0005	0.25	1
O	8c	0.129	0.177	0.273	1
O	8c	0.116	0.794	0.281	1
O	4a	0.629	0	0	1
O	4a	0.365	0	0	1
O	4a	0.057	0	0	1

TABLE II. Starting model of $Gd_{2.85}SbO_7$:*0.15*Eu^{3+}

Element	Wyckoff	*x*	*y*	*z*	Sof
Gd	4a	0	0	0	0.7125
Eu	4a	0	0	0	0.0375
Sb	4a	0	0	0	0.25
O	8c	0.25	0.25	0.25	1

TABLE III. Refined parameters of Rietveld analysis of $Gd_{2.85}MO_7$:*0.15*Eu^{3+} (M = Nb, Sb, Ta)

Sample	**M = Nb**	**M = Sb**	**M = Ta**
Crystal Structure	Orthorhombic	Cubic	Orthorhombic
Space group	C2221	F*m*-3*m*	C2221
Flat background	117.4537	116.2166	125.8454
Coefficient 1	-17.6815	-17.3529	-23.4959
Coefficient 2	19.3853	17.9869	22.46233
Scale Factor	0.0000	0.0001	0.000007
Lattice parameters			
***a* [Å]**	10.6035(4)	5.3251(2)	10.6308(5)
***b* [Å]**	7.5175(3)	5.3251(2)	7.5249(3)
***c* [Å]**	7.5348(2)	5.3251(2)	7.5430(4)
Cagliotic parameters			
U	0.2688	0.1350	0.197534
V	-0.1531	-0.0165	-0.093856
W	0.0265	0.0105	0.018997
Asymmetry parameter	1.2454	0.5004	0.416902
Peak Shape 1	0.6545	0.5463	0.88169
Peak Shape 2	0.0003	0.0000	-0.008244
Residual parameters			
Rexp (%)	8.40	8.45	7.92
Rp (%)	7.55	7.28	6.76
Rwp (%)	10.02	9.37	8.70
GOF	1.42	1.22	1.20

TABLE IV. Selected bond distances of $Gd_{2.85}MO_7$:*0.15*Eu^{3+} (M = Nb, Ta)

M=Nb			M=Ta		
Gd	- O3	2.328	Gd1	- O3	2.332
	- O4	2.366		- O4	2.37
	- O2	2.57		- O2	2.574
	- O1	2.762		- O1	2.766
Gd2	- O4	2.248	Gd2	- O4	2.252
	- O3	2.282		- O3	2.285
	- O2	2.325		- O2	2.327
	- O1	2.352		- O1	2.358
	- O1	2.365		- O1	2.366
	- O2	2.481		- O2	2.487
	- O5	2.575		- O5	2.58
Nb	- O1	1.919	Ta	- O1	1.922
	- O5	1.978		- O5	1.981
	- O2	1.988		- O2	1.991
O1	- Nb	1.919	O1	- Ta	1.922
	- Gd2	2.352		- Gd2	2.358
	- Gd2	2.365		- Gd2	2.366
	- O5	2.566		- O5	2.569
	- O1	2.758		- O1	2.764
	- Gd	2.762		- Gd1	2.766
	- O2	2.872		- O2	2.879
	- O2	2.883		- O2	2.886
	- O5	2.93		- O5	2.935
	- O4	2.971		- O4	2.974
	- O3	3.182		- O3	3.185
	- O3	3.359		- O3	3.365
	- O2	3.37		- O2	3.374
O2	- Nb	1.988	O2	- Ta	1.991
	- Gd2	2.325		- Gd2	2.327
	- Gd2	2.481		- Gd2	2.487
	- O2	2.504		- O2	2.51
	- Gd	2.57		- Gd1	2.574
	- O5	2.697		- O5	2.7
	- O4	2.766		- O4	2.768
	- O1	2.872		- O1	2.879
	- O1	2.883		- O1	2.886
	- O5	2.913		- O5	2.918
	- O3	3.064		- O3	3.067
	- O1	3.37		- O1	3.374
O3	- Gd2	2.282	O3	- Gd2	2.285
	- Gd	2.328		- Gd1	2.332
	- O4	2.799		- O4	2.806
	- O2	3.064		- O2	3.067
	- O1	3.182		- O1	3.185
	- O1	3.359		- O1	3.365
O4	- Gd2	2.248	O4	- Gd2	2.252
	- Gd	2.366		- Gd1	2.37
	- O2	2.766		- O2	2.768
	- O3	2.799		- O3	2.806
	- O1	2.971		- O1	2.974
	- O5	3.266		- O5	3.274
O5	- Nb	1.978	O5	- Ta	1.981
	- O1	2.566		- O1	2.569
	- Gd2	2.575		- Gd2	2.58
	- O2	2.697		- O2	2.7
	- O2	2.913		- O2	2.918
	- O1	2.93		- O1	2.935
	- O4	3.266		- O4	3.274

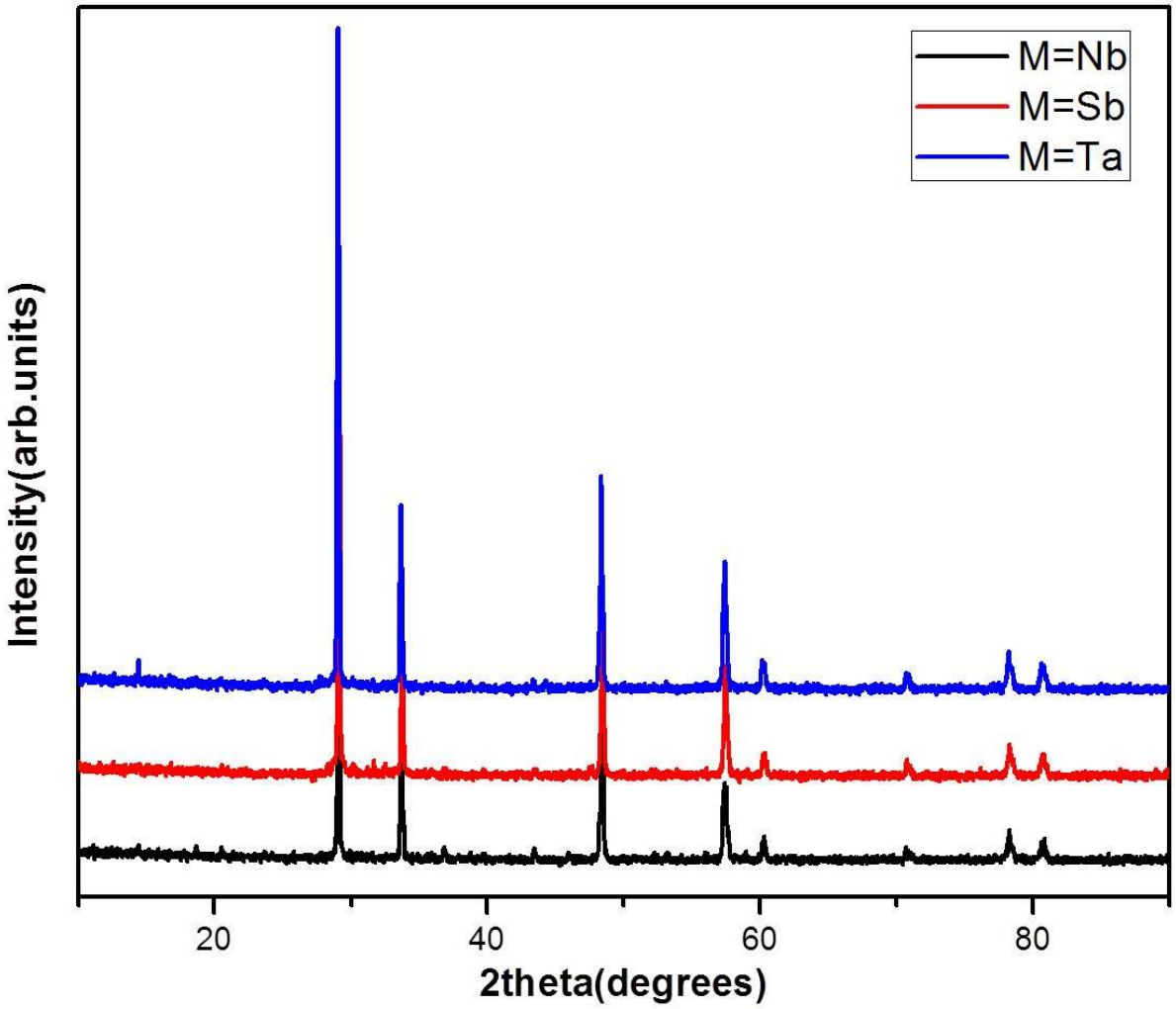

FIG. 1.Powder X-ray diffraction patterns of $Gd_{2.85}MO_7$:*0.15*Eu^{3+} (M = Nb, Sb, Ta)

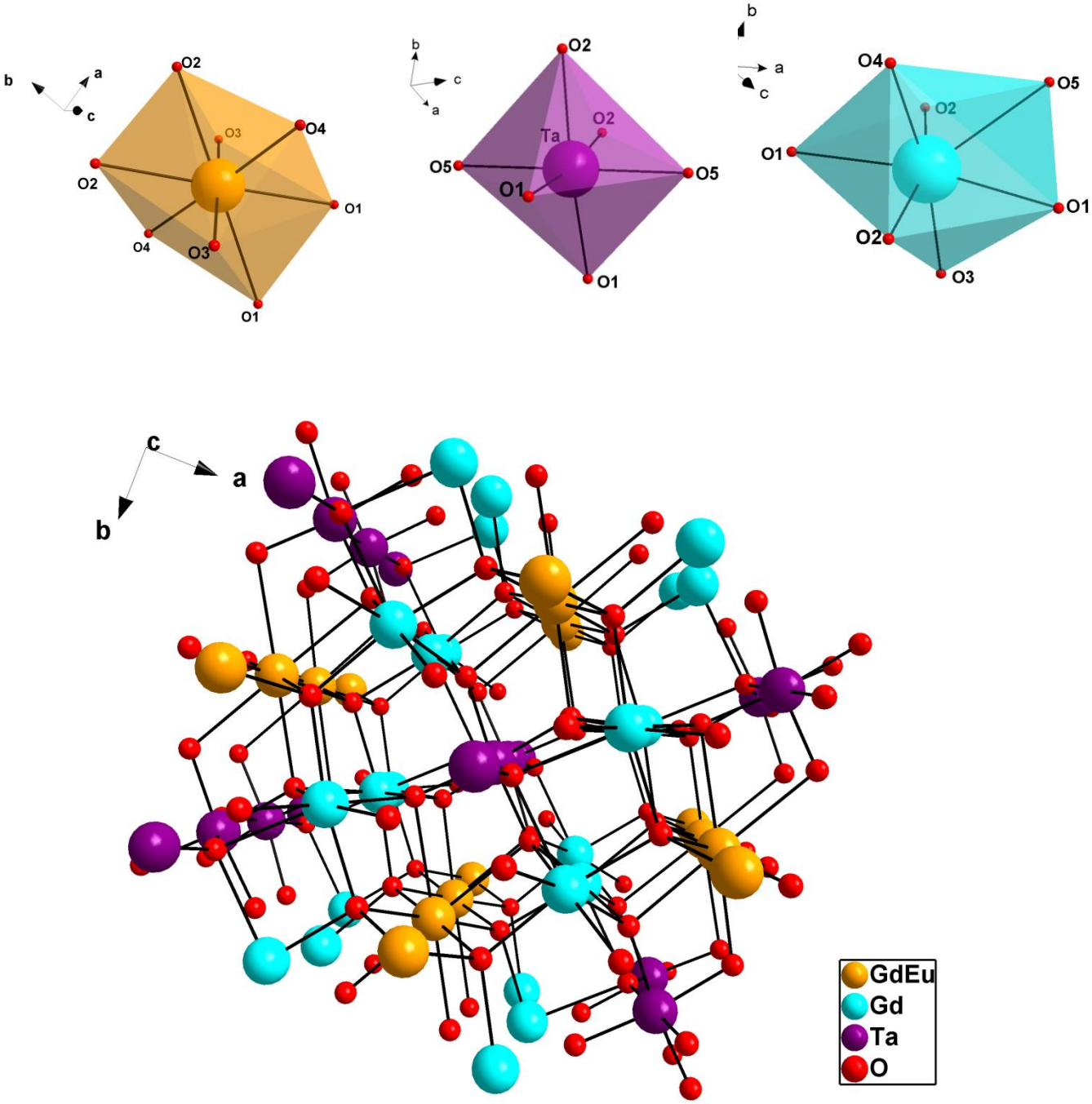

FIG. 2. Schematic representation of the crystal structure and the coordination polyhedras of $Gd_{2.85}TaO_7$:*0.15*Eu^{3+} .

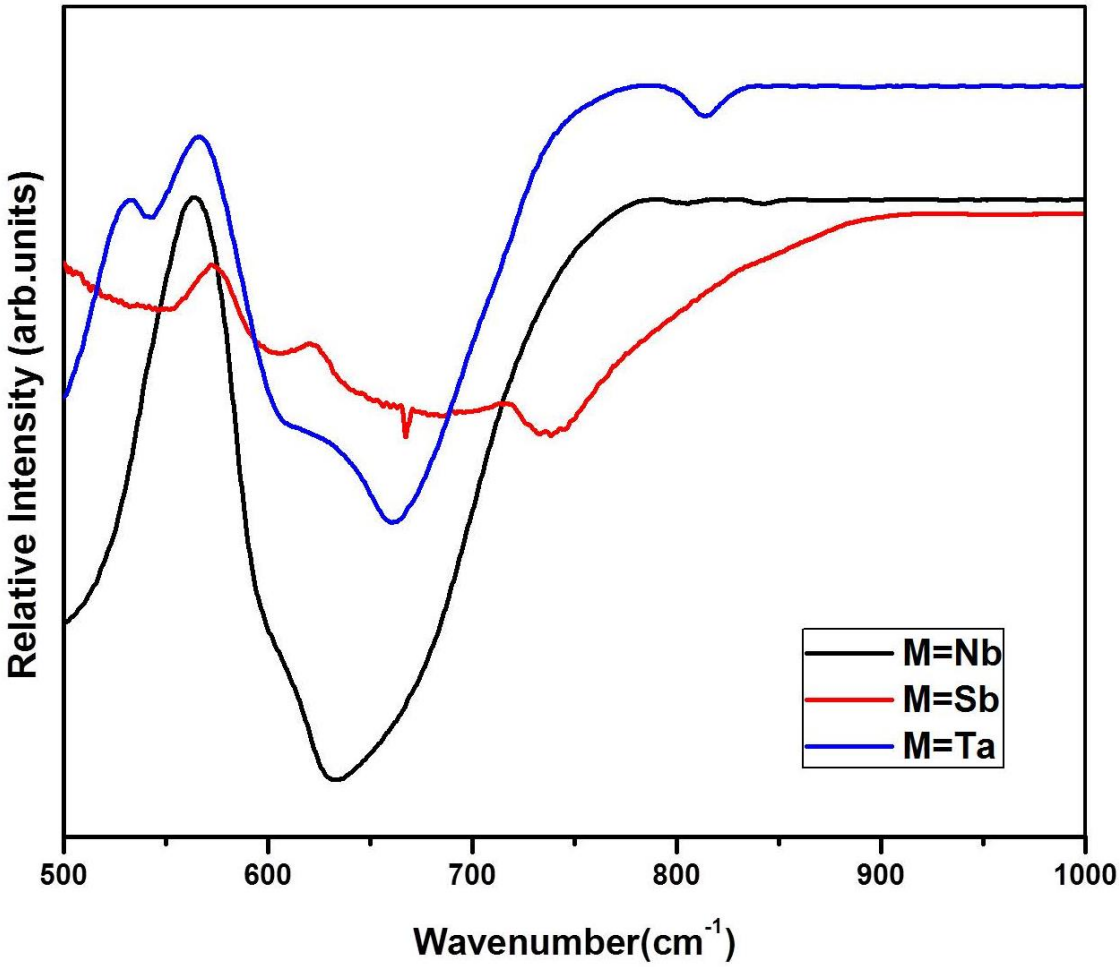

FIG. 3.FT - IR Spectra of $Gd_{2.85}MO_7$:*0.15*Eu^{3+} (M = Nb, Sb, Ta) samples.

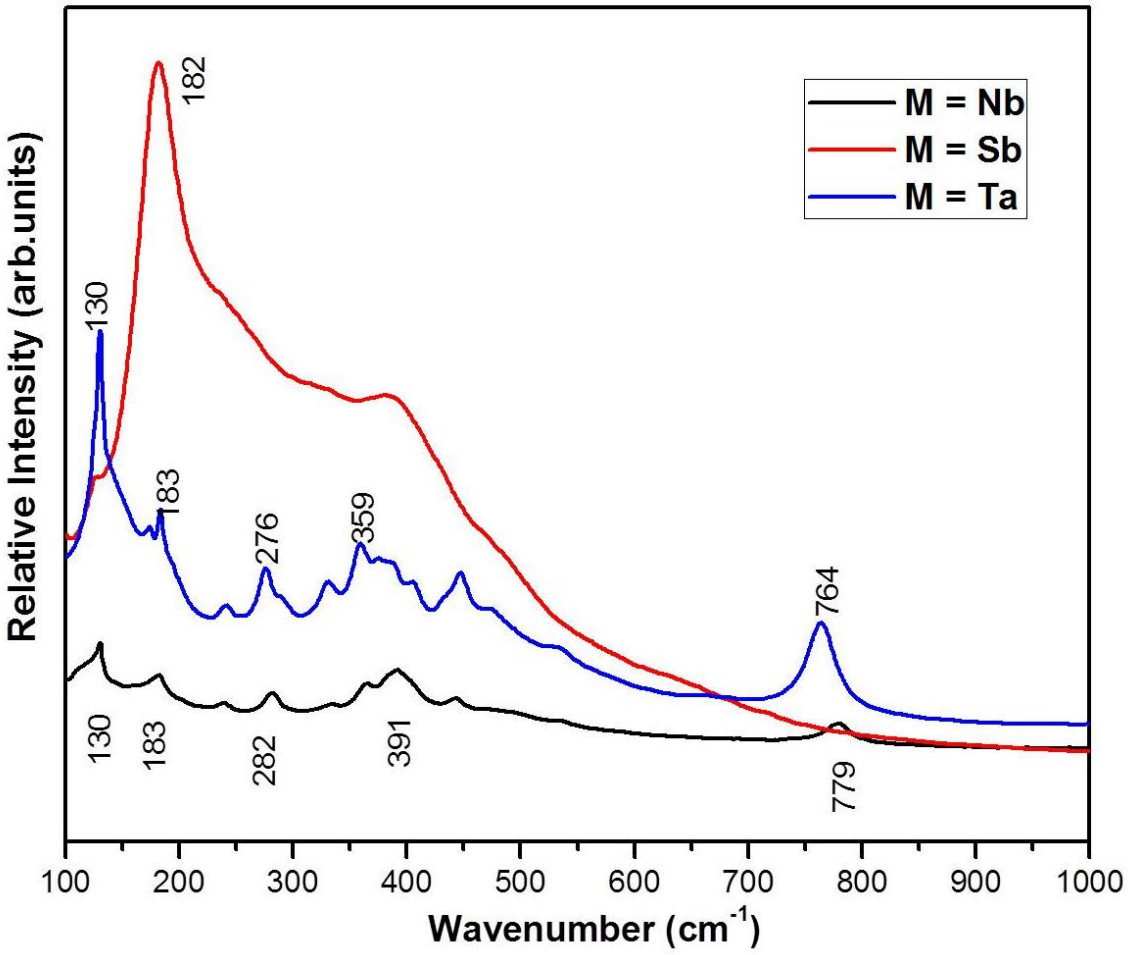

FIG. 4.FT Raman Spectra of $Gd_{2.85}MO_7$:*0.15*Eu^{3+} (M = Nb, Sb, Ta) samples.

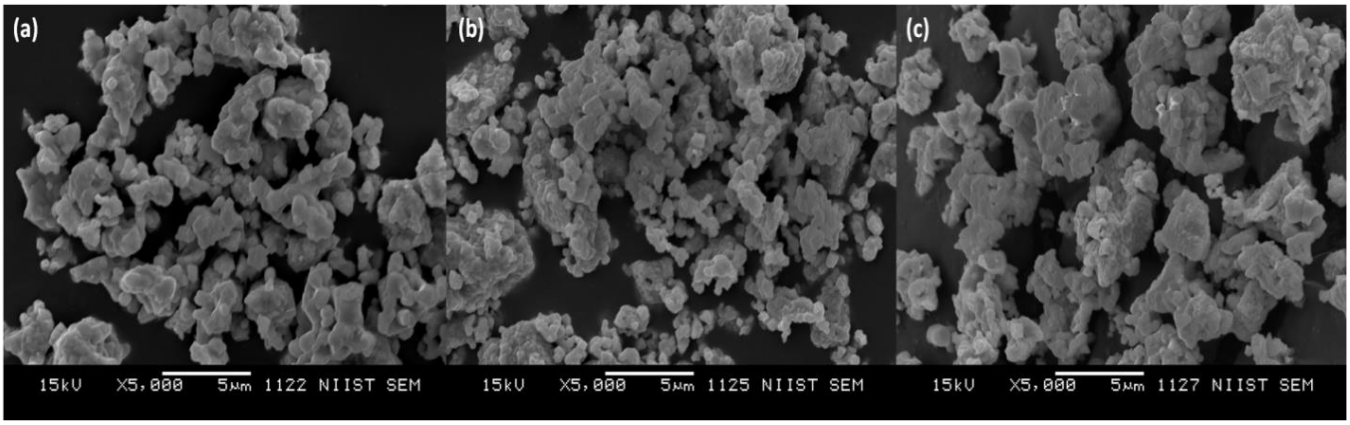

FIG. 5.Scanning electron micrographs of $Gd_{2.85}MO_7$:*0.15*Eu^{3+} M = Nb (a), Sb (b), Ta (c)

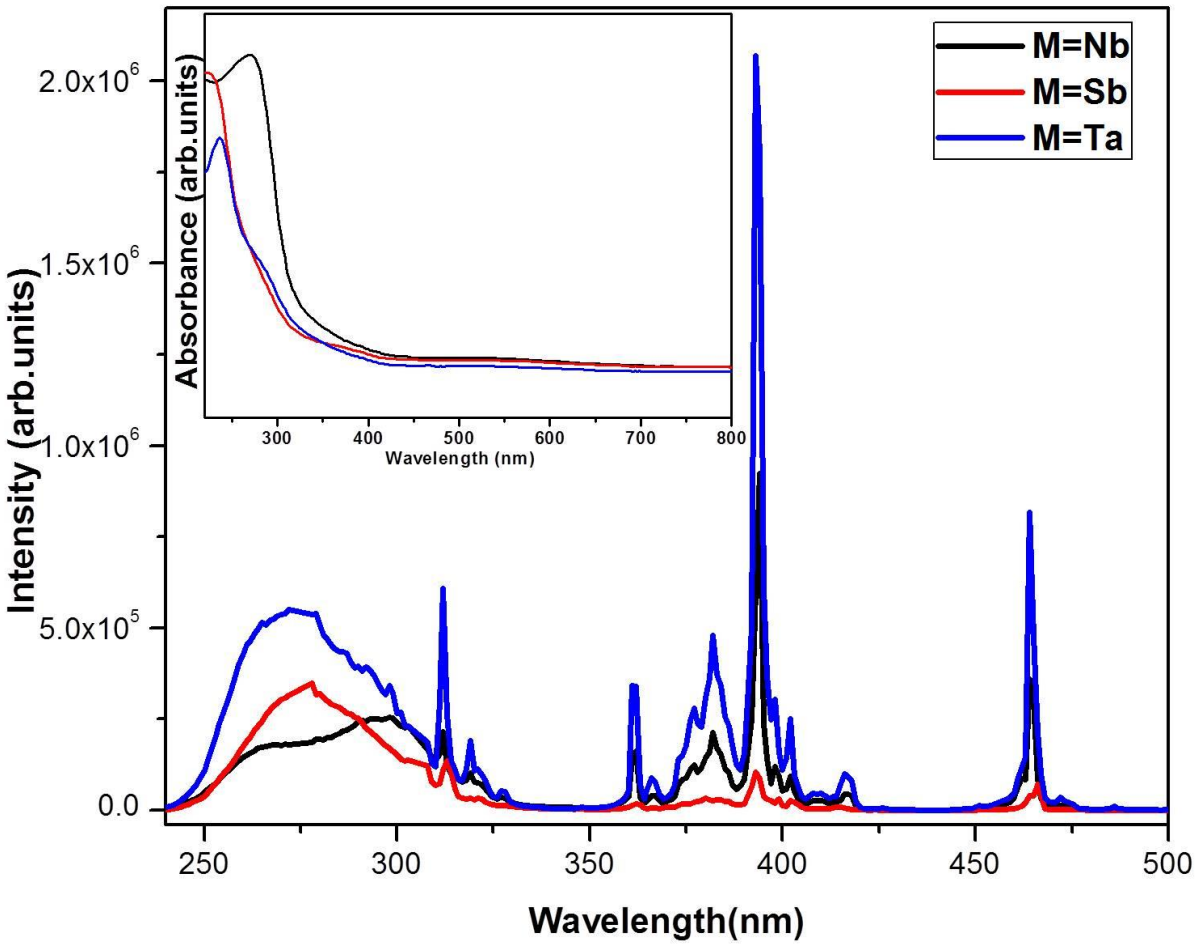

FIG. 6.Photoluminescence excitation spectrum of $Gd_{2.85}MO_7$:*0.15*Eu^{3+} (M = Nb, Sb, Ta) for an emission at 612 nm (Inset: UV - Visible absorption spectrum of the samples)

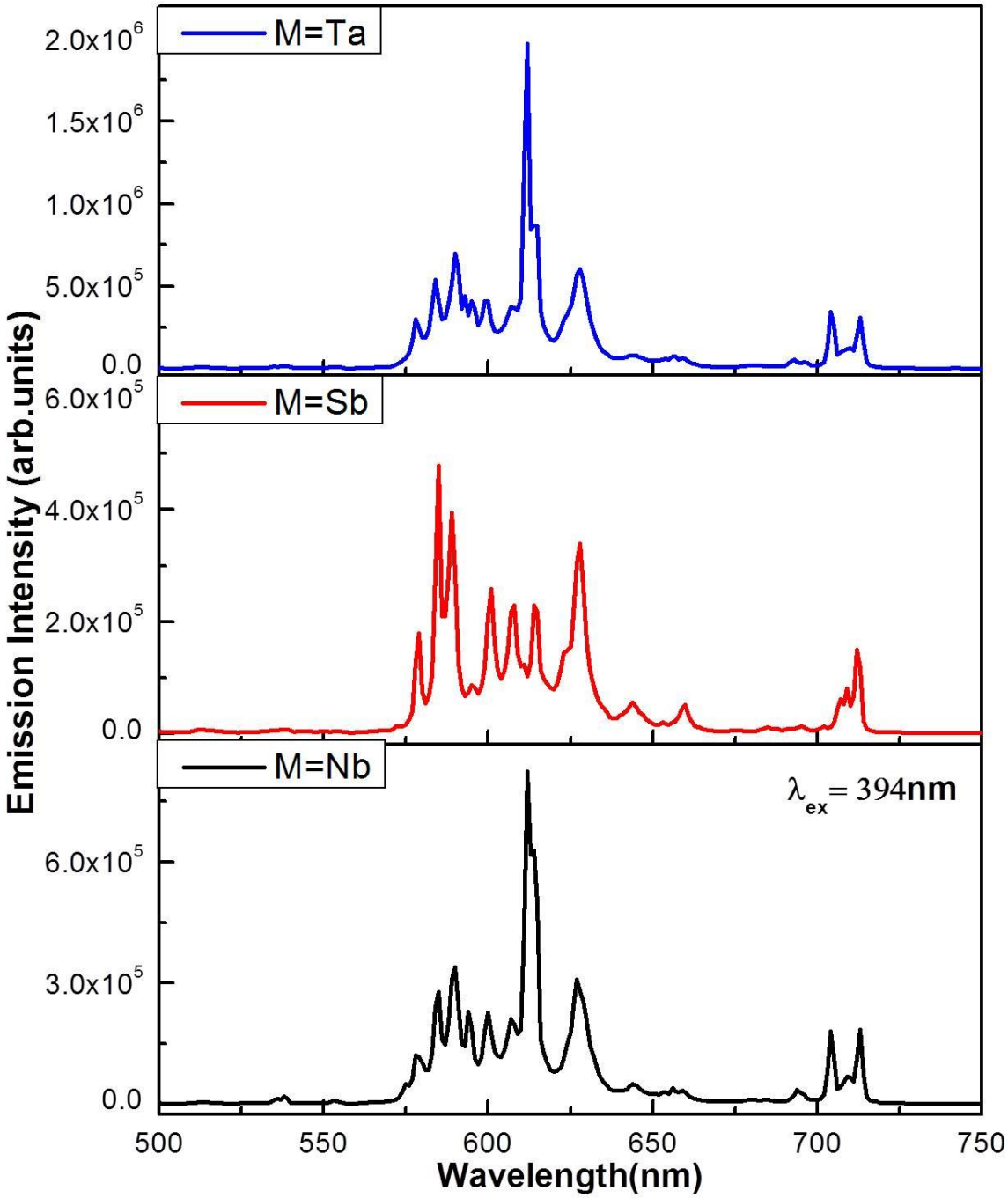

FIG. 7.Photoluminescence emission spectra of $Gd_{2.85}MO_7$:*0.15*Eu^{3+} (M = Nb, Sb, Ta) under 394 nm excitation

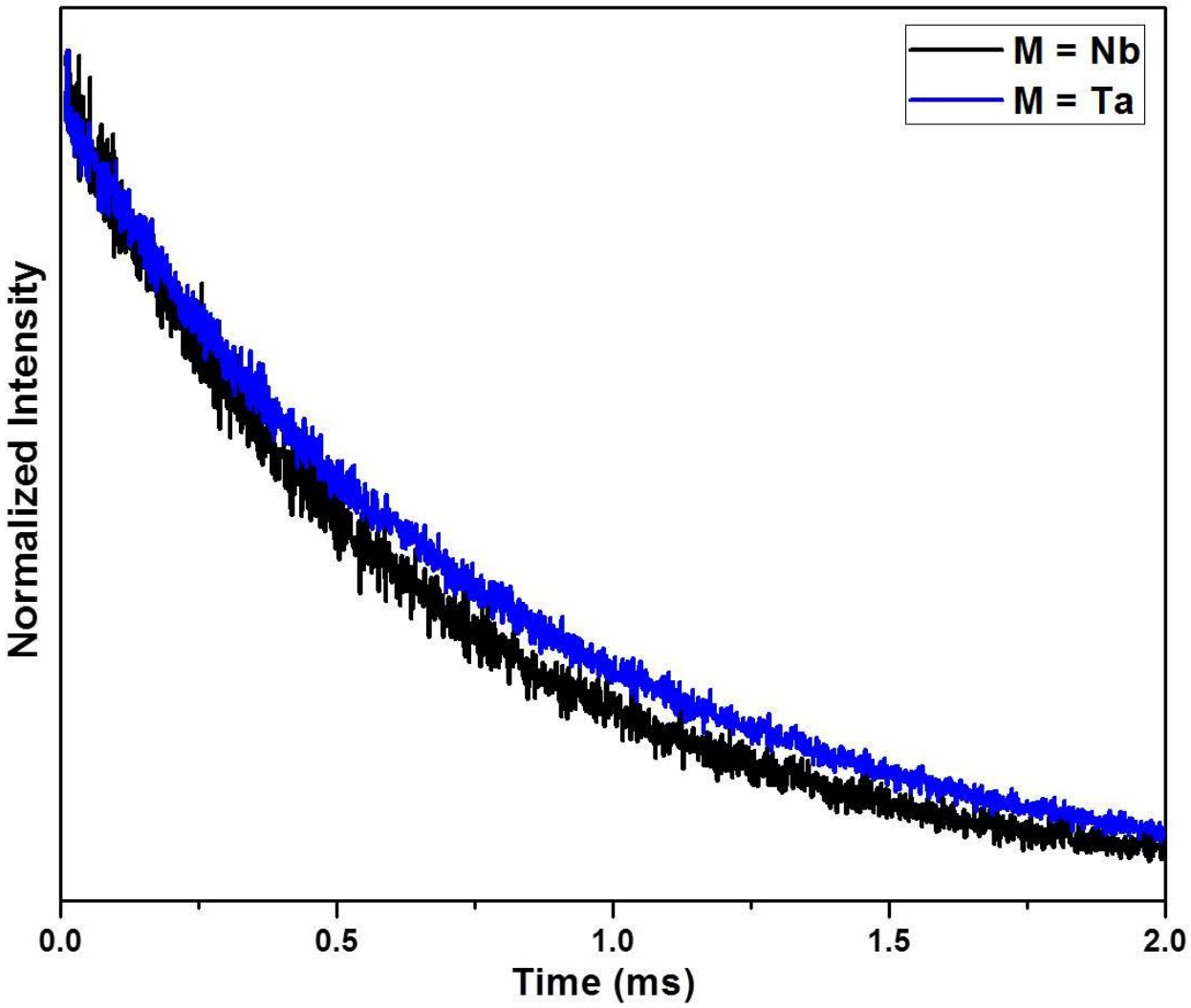

FIG. 8.Decay curves of Eu^{3+} emission at 612 nm in $Gd_{2.85}MO_7$:*0.15*Eu^{3+} (M = Nb, Ta) under 394 nm excitation.

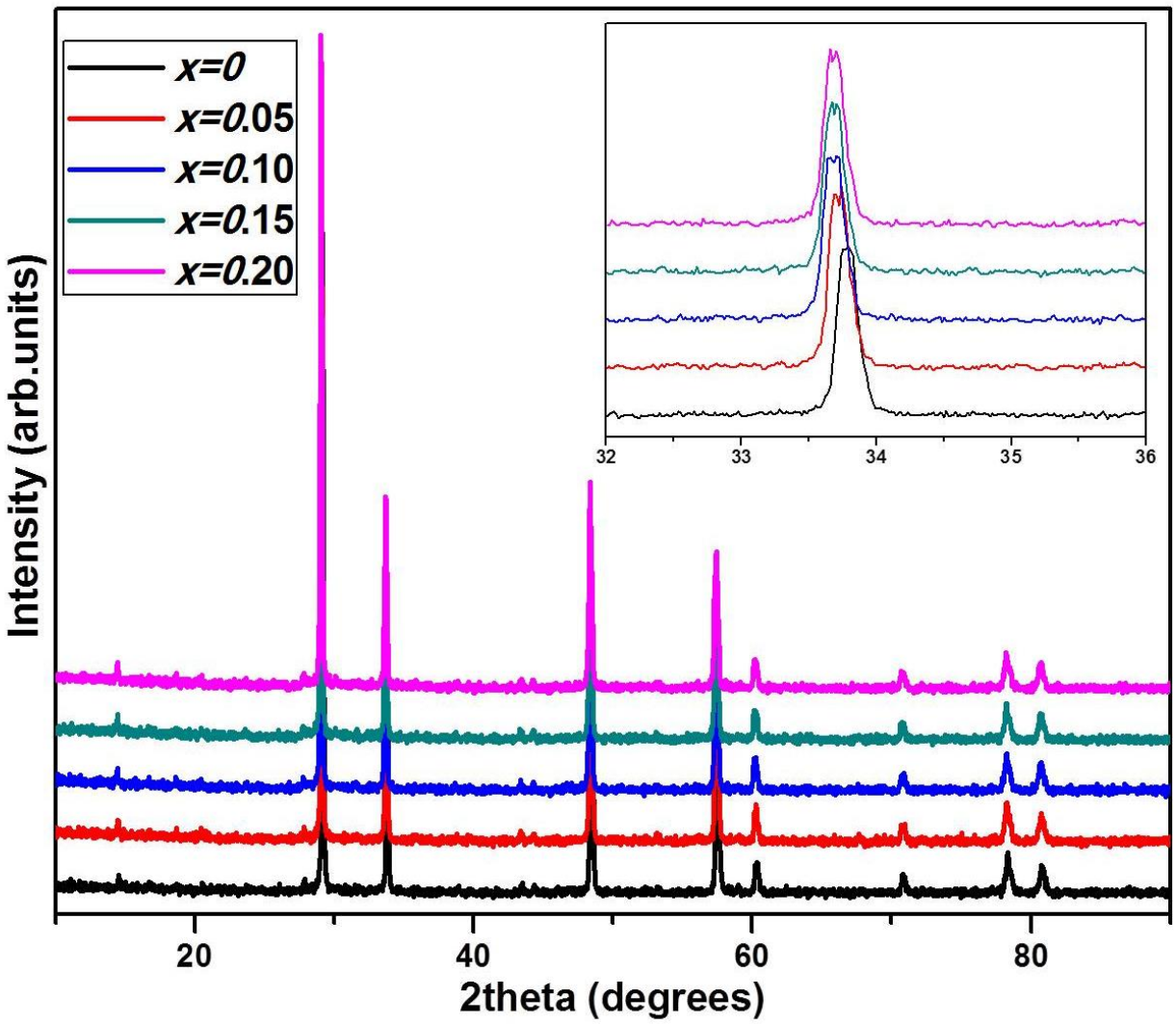

FIG. 9.Powder X-ray diffraction patterns of $Gd_{3-x}TaO_7:xEu^{3+}$ (x = 0.05, 0.1, 0.15, 0.2)

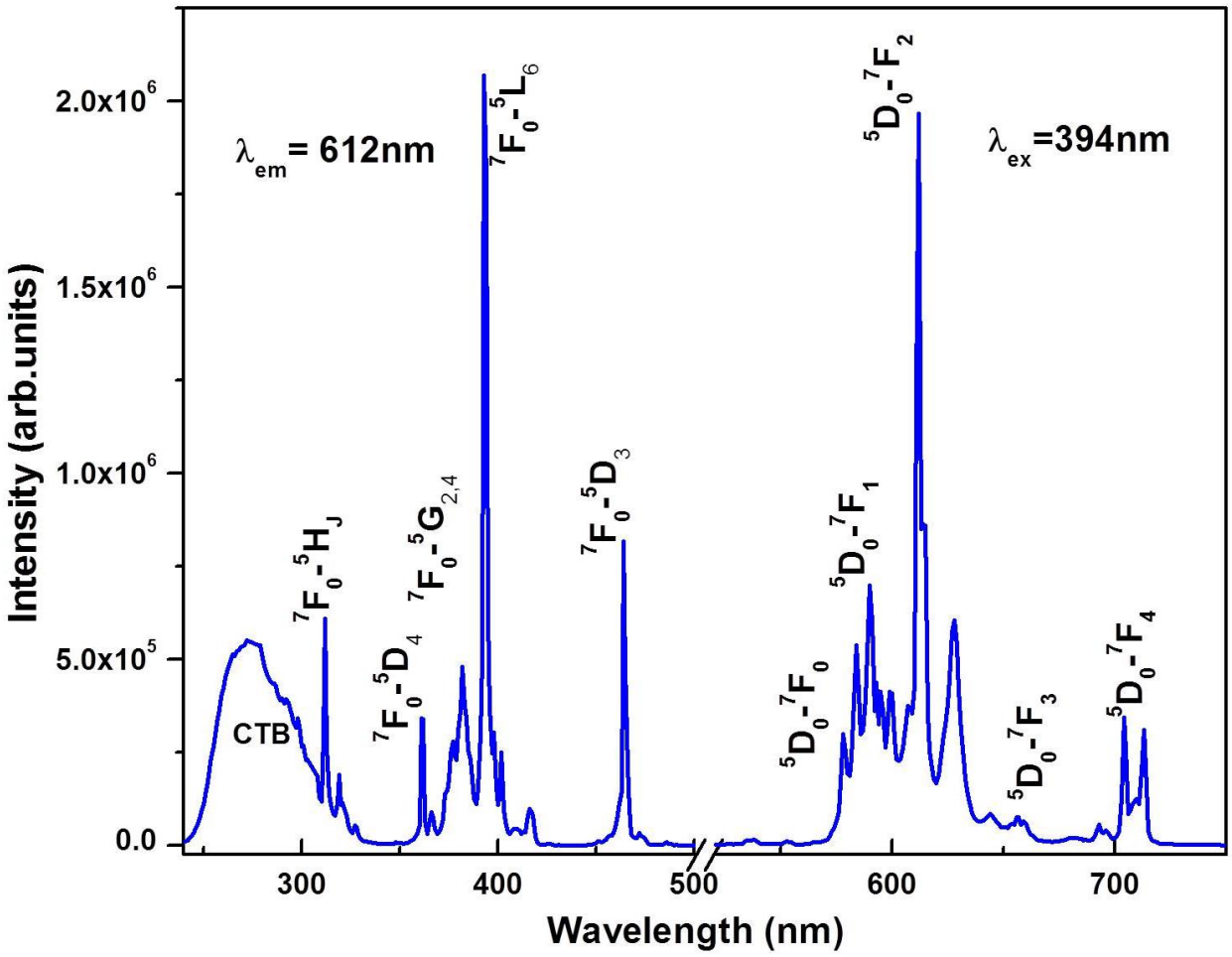

FIG. 10.Photoluminescence emission spectra under 394 nm excitation and excitation spectrum for an emission at 612 nm of $Gd_{2.85}TaO_7$: *0.15*Eu^{3+}

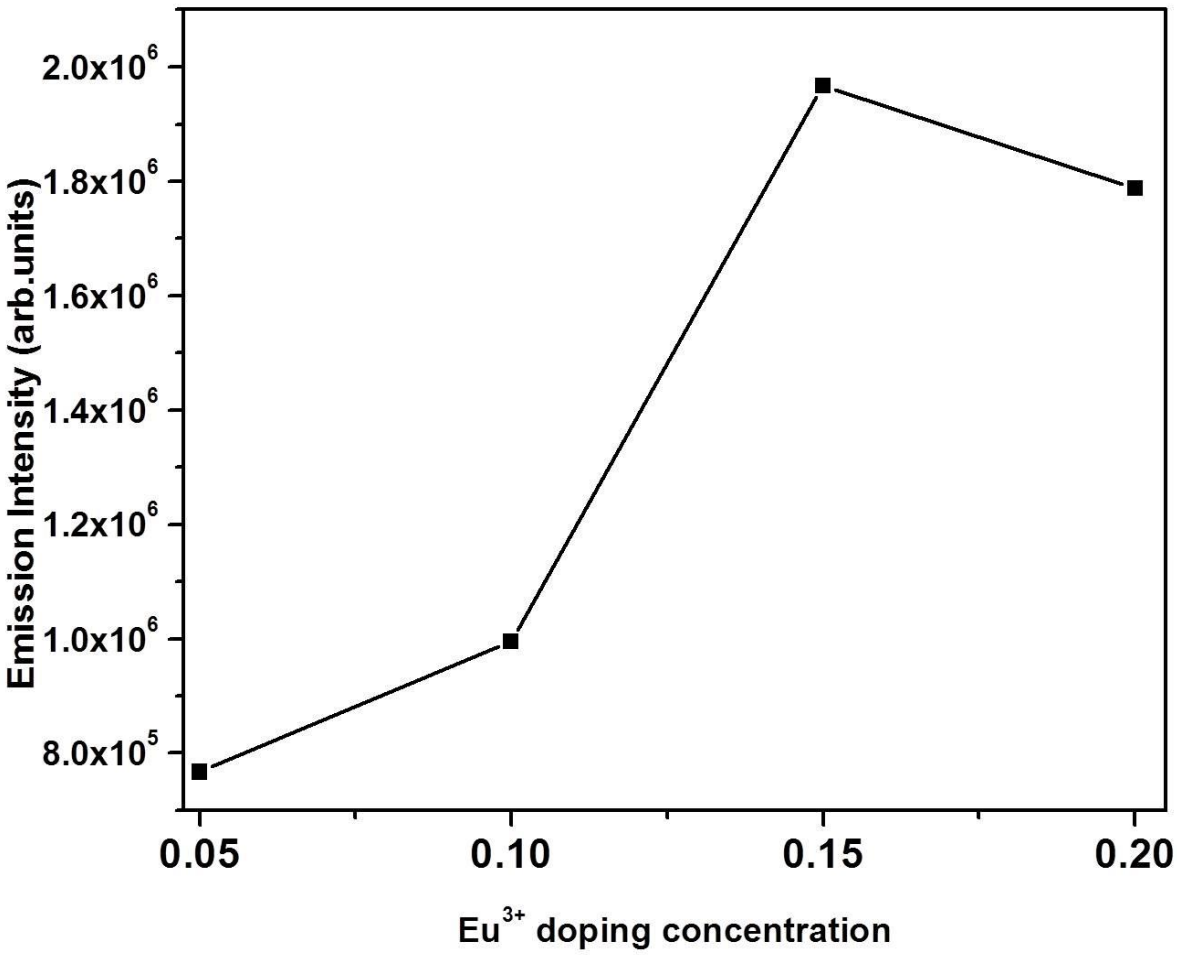

FIG. 11.Variation in luminescent intensities of $Gd_{3-x}TaO_7:xEu^{3+}$ (x = 0.05, 0.1, 0.15, 0.2) with Eu^{3+} doping concentrations

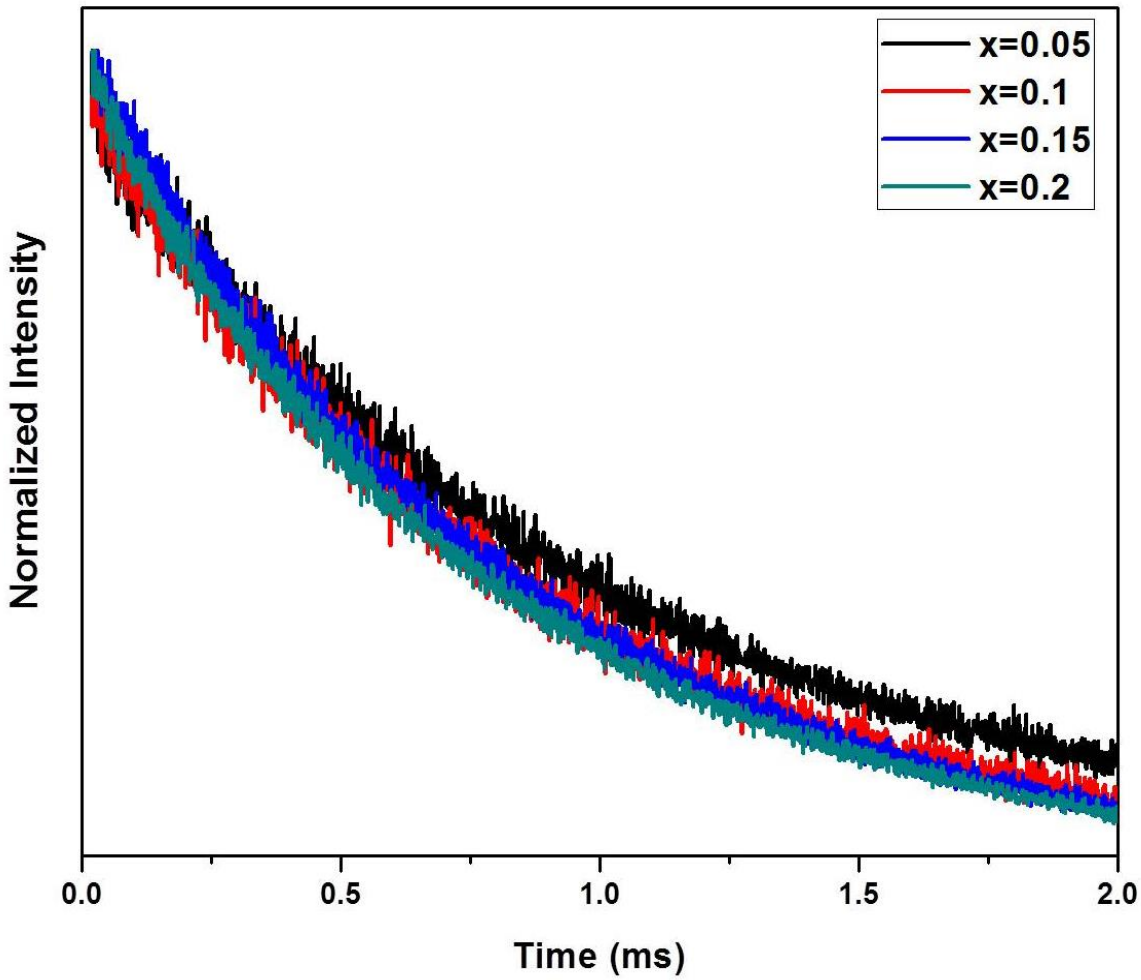

FIG. 12.Decay curves of Eu^{3+} emission at 612 nm in $Gd_{3-x}TaO_7:xEu^{3+}$ (x = 0.05, 0.1, 0.15, 0.2) under 394 nm excitation.